

Using lateral dispersion to optimise microfluidic trap array efficiency

Nicolas Ruysse^{*,1}, Gabriel Fina^{2,3}, Rachele Allena^{4,5}, Marie-Caroline Jullien⁶, and Jacques Fattaccioli^{2,3}

¹Sorbonne Université, Physico-Chimie des Electrolytes et Nanosystèmes Interfaciaux, PHENIX, CNRS UMR 8234, Paris F-75005, France

²PASTEUR, Département de Chimie, École Normale Supérieure, PSL Université, Sorbonne Université, CNRS, 75005 Paris, France

³Institut Pierre-Gilles de Gennes pour la Microfluidique, 75005 Paris, France

⁴Université Côte d'Azur, Laboratoire Jean Alexandre Dieudonné UMR CNRS 7351, Nice, France

⁵Institut Universitaire de France

⁶Univ. Rennes, CNRS, IPR (Institut de Physique de Rennes) UMR 6251, F-35000 Rennes

Keywords Microfluidics, trapping, optimisation, CFD

Abstract

Microfluidic trapping arrays have proven to be efficient tools for various applications that require working at the single-cell level, such as cell-cell communication or fusion. Although several hydrodynamic trapping devices have already been optimised, two-dimensional (2D) single-layer trapping arrays with high trap densities remain partially inefficient. Specifically, many traps remain empty, even after prolonged injection, which drastically reduces the number of samples available for post-treatment. These unfilled traps result from the symmetrical nature of the flow around the traps, and breaking this symmetry enhances capture efficiency. In this study, we use a numerical approach to show that optimal geometries can significantly increase filling efficiency and a preliminary experimental test confirming our approach is provided. We show that these improvements are achieved by promoting lateral dispersion of particles, facilitated either through an optimised oblique flow or by introducing disorder into the spatial arrangement of traps without specific inlet/outlet adjustment.

*Corresponding author: nicolas.ruysse@sorbonne-universite.fr

1 Introduction

Microfluidic trapping arrays are of significant interest due to their capacity to precisely capture and manipulate individual cells or particles within a highly controlled environment. These arrays enable high-throughput analysis and long-term observation, both essential for advancing research in cell biology, drug screening, and diagnostics. Over the years, a broad range of technical solutions has been developed: trapping can be achieved passively through gravity [1, 2, 3, 4], inertial lift [4], or permanent magnets [5, 6], as well as through active methods such as valves [7, 8], optical tweezers [9], dielectrophoresis [10, 11], electromagnets [12], or acoustics [13]. Among these methods, hydrodynamic trapping arrays are the simplest, operating by suspending objects in a fluid that flows through a microfluidic chamber containing an array of traps. Since the objects targeted for immobilization follow the fluid flow, they are captured in these traps, either individually or in quantities that depend on the size ratio between the target objects and the traps. Thanks to their apparent simplicity in implementation and relative ease in terms of microfabrication, the literature attached to hydrodynamic arrays is vast.

The optimisation of trapping efficiency relies on tailoring the flow inside the chamber which goes through the trapping array. The most common hydrodynamic trapping arrays so far consist of two-dimensional (2D) systems with traps arranged in a regular staggered pattern within a Hele-Shaw cell [14, 15, 16, 17, 18]. Although several hydrodynamic trapping devices have been optimised, trapping arrays made by single-layer lithography remain only partially efficient. Indeed, many traps frequently remain empty even after prolonged injection, which significantly reduces the number of samples available for further analysis [17]. Trapping efficiency improves with double-layer lithography techniques [14, 15, 18], though this method complicates fabrication.

Recently, we have demonstrated that both the efficiency and trapping homogeneity of microfluidic arrays, fabricated via single-layer lithography, can be significantly improved by tailoring the flow within the chamber through precise inlet and outlet positioning [19]. This configuration directs the carrier fluid to flow diagonally relative to the chamber's main axis, inducing flow asymmetry in front of each trap, which enhances particle immobilization probability. Additionally, most numerical studies rely on 3D [4, 17, 20, 21, 22] or 2D with explicit solid particles [21, 23, 24] models which both are too computationally intensive for an optimisation study of dense trapping arrays (of approximately 100 traps). we have achieved strong agreement with experimental results using a simplified 2D Computational Fluid Dynamics (CFD) approach, enabling an increase in the number of geometries studied with minimal computational cost [19].

In this study, we investigate how trapping efficiency and homogeneity can be optimised. Firstly, we optimise trapping efficiency independently across five dimensionless geometric parameters. Secondly, we demonstrate by simulation that comparable trapping efficiencies can be obtained with disordered trapping arrays and experimentally verify the potential of such geometries for one example. Finally,

we conduct a quantitative analysis of the lateral dispersion of Lagrangian particles within the optimised geometries. This analysis confirms the critical role of lateral dispersion in facilitating large-scale particle trapping. These comprehensive results enable us to identify the most important parameters to consider for achieving efficient trapping arrays and to gain a deeper understanding of the underlying mechanisms that enhance trapping efficiency.

2 Materials and methods

2.1 Parameterised geometry

The whole numerical model is developed using the commercial Finite-Element software COMSOL Multiphysics® while post-processing is achieved with Python. We study a single layer trapping array of 98 traps as previously [19]. Because of symmetry, a 2D model built from parameterised geometric primitives is suggested (Figure 1). The trapping array is initially organised in a rectangular staggered pattern of axis (Ox) in the streamwise direction and of axis (Oy) in the lateral direction, (see Figure 1 where all the geometrical parameters were sketched). The dimensions of the trapping array are l and w and the one of the cavity are L and W in the streamwise resp. lateral directions; and the distances between the traps are respectively Δx and Δy . We call "chamber" the whole system including the trapping array and the cavity. For more information, all the fixed geometric parameters of the model are reported in supplementary Table 1 section 8.1.

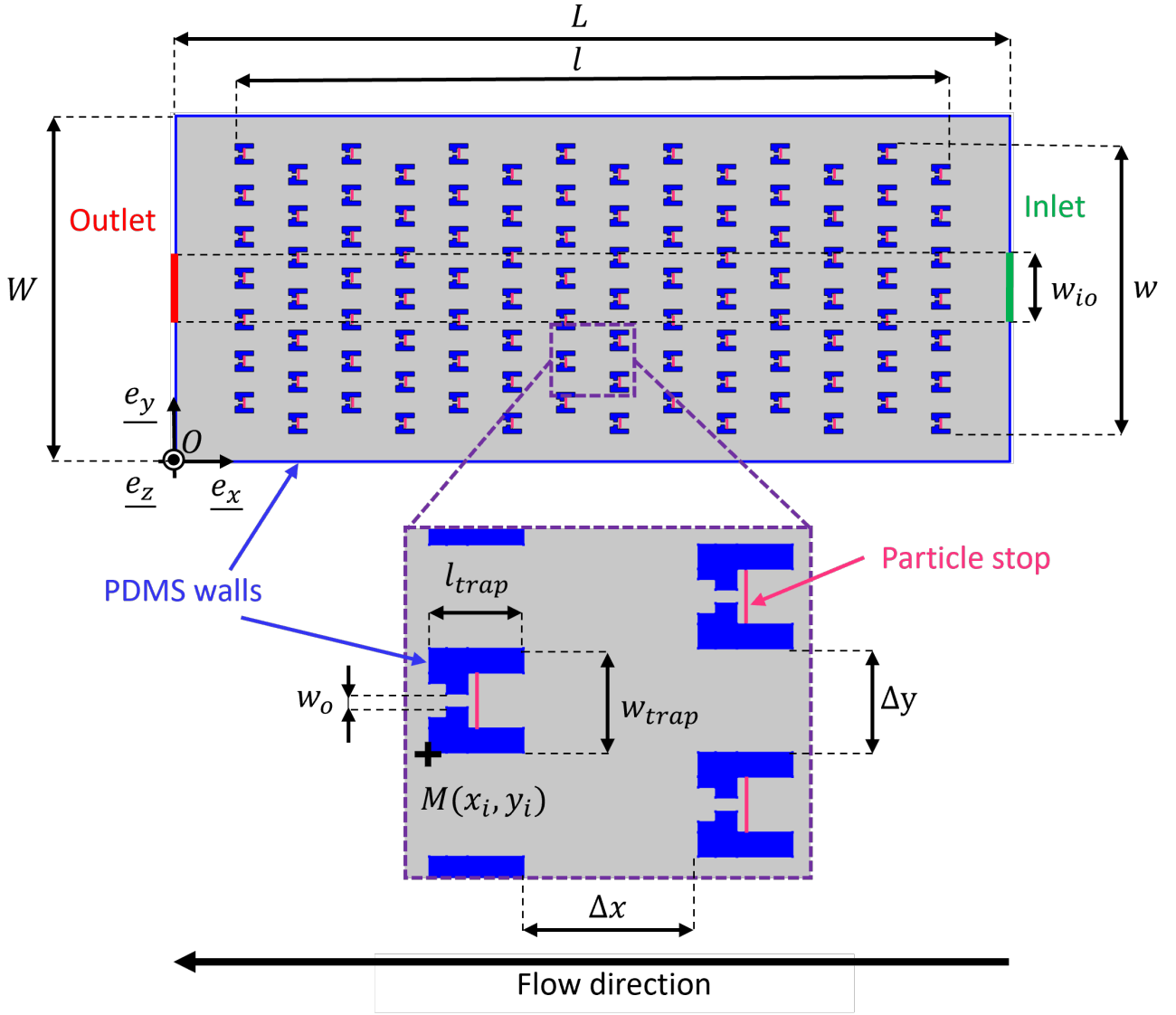


Figure 1: The model geometry. The fluid domain is represented in grey, the traps and the PDMS walls in blue, the inlet resp. outlet channels in green resp. in red. A particle stop frontier is added in each trap (in pink) to virtually stop particles without modifying the fluid flow.

2.2 Physics of the problem

We consider the flow as incompressible, stationary and the fluid as Newtonian. Furthermore, the maximal Reynolds number $Re = \frac{Uh}{\nu}$ (where $U \sim 1 \text{ mm s}^{-1}$ is the maximal mean velocity, $h = 14 \text{ }\mu\text{m}$ the height of the cavity and $\nu = 10^{-6} \text{ m}^2 \text{ s}^{-1}$ the kinematic viscosity of the solution) is about $Re = 0.01$, which allows us to consider the Stokes equations. In order to simplify the study, the fluid flow is reduced in 2D in the in-plan of the cavity (*i.e.* $(O, \underline{e}_x, \underline{e}_y)$, Figure 1) and verifies the Brinkman equations that account for both viscous dissipation in the in-plane and in the out-of-plane direction of the cavity (*ie*

(O, \underline{e}_z), Figure 1) through a body force \underline{f} . As such, the latter equations read:

$$\begin{cases} -\nabla p + \mu \nabla^2 \underline{v} + \underline{f} = \underline{0} \\ \nabla \cdot \underline{v} = 0 \end{cases} \quad (1)$$

where p is the pressure field, μ the fluid dynamic viscosity, \underline{v} the velocity field. The chamber is horizontally orientated such that gravity does not contribute to the flow. The friction body force \underline{f} is given in the shallow channel approximation by:

$$\underline{f} = -\frac{12\mu}{h^2} \underline{v} \quad (2)$$

Therefore, \underline{v} corresponds to the depth-averaged velocity field in-plane (in 2D). As boundary conditions, uniform pressures were applied on the inlet $p_{in} = 100$ Pa and outlet $p_{out} = 0$ Pa boundaries. On the PDMS walls, the viscous fluid-solid interaction forces a zero fluid velocity $\underline{v} = \underline{0}$. First, equations 1, 2 and the latter boundary conditions are numerically solved to calculate the stationary flow \underline{v} . To do so, these equations are translated into a mixed weak formulation and are discretised in space by applying the Finite-Element Method (FEM) with linear Lagrange interpolation functions for both pressure and velocity fields. For more information see supplementary section 8.2.

We study a dispersion of polystyrene (PS) particles of diameter $D_p = 5$ μm and of concentration $C_p = 10^6$ ml^{-1} . This concentration is sufficiently small that particles do not modify the viscosity of the suspending fluid and leads to a typical distance between particles about 62 μm which allows to neglect particle-particle interactions. Furthermore, the particles diffusion coefficient is about $8.7 \cdot 10^{-14}$ $\text{m}^2 \text{s}^{-1}$ which makes particle diffusion negligible with respect to particle convection. Despite a low Reynolds number, the Lifo-Diffusif number was $\mathcal{N} = \frac{27\pi V^2 \rho R_p^4}{2k_b T h} \sim 30$, thus, lift forces are non-negligible in our flow conditions [25]. However, the corresponding maximal depletion thickness at the outlet of the chamber is $\delta = \sqrt{\frac{R_p \rho L}{Wh^2 \mu}} \sim 1.3$ μm which is small compared the particle size of 5 μm , such deviations is thus disregarded in the following. The PS particles density of 1.05 g ml^{-1} is very close to the carrier fluid one, thus particle sedimentation is also disregarded. As the Reynolds number is low and the particles are three times smaller than the channel height, we make the assumption that the particle center of mass trajectories were similar to the carrier fluid streamlines (neglected size). The particles equation of motion is obtained considering a purely advective transport:

$$\frac{\partial \underline{r}}{\partial t} = \underline{v} \quad (3)$$

where \underline{r} is the particle position. When a particle enters into a trap, it is artificially stopped at a stop boundary in each trap (pink boundaries Figure 1). Experimentally, it is impossible to perfectly control the particle initial positions at the inlet. Therefore, we try to sweep the most possible every positions on the inlet by regularly placing $N_p = 200$ ($\approx 2 \times$ number of traps) particles on the inlet boundary. Equation

3 is discretised in time and integrated using an implicit generalised-alpha numerical scheme.

2.3 Geometry parametric analysis

From a purely applications perspective, the reader can refer to sections 3.2 outlining the optimum characteristics of a high-performance trapping array. This section presents the definition of the different parameters that are used for the optimisation of the trapping array. We first have to define the objective of the optimisation. As several particles can be captured in a same trap, we make a distinction between the filling efficiency E_{fill} i.e. the proportion of occupied traps by at least one particle:

$$E_{fill} = \frac{\text{number of occupied traps}}{\text{number of traps}} \quad (4)$$

and the capture efficiency E_{capt} i.e. the proportion of trapped particles:

$$E_{capt} = \frac{\text{number of trapped particles}}{\text{number of particles}} \quad (5)$$

Since the number of particles (~ 2 number of traps) is greater than the number of traps, we can expect that $E_{fill} > E_{capt}$. In order to optimise these objectives, several dimensionless geometric parameters, defined arbitrarily by us, have been varied:

- The centering C represents the shift between the inlet and outlet channels in the lateral direction and thus allows studying symmetry/asymmetry effects between the inlet and the outlet. Its value is 100% when the inlet and the outlet were perfectly aligned (as in Figure 1) and 0% when the shift is maximal. C is given by:

$$C = 1 - \frac{\Delta y_{io}}{\Delta y_{io \max}} = 1 - \frac{2 \Delta y_{io}}{W - w_{io}} \quad (6)$$

where Δy_{io} is the lateral distance between the inlet and outlet and $\Delta y_{io \max}$ is its maximal value.

- The width ratio W_r in the lateral direction between the trap array and the cavity width is defined by:

$$W_r = \frac{w}{W} \quad (7)$$

This ratio allows to investigate the role of a particle bypass on the sides of the cavity.

- The length ratio L_r in the stream direction between the trap array and the cavity length is defined by:

$$L_r = \frac{l}{L} \quad (8)$$

This ratio allows investigating possible entrance effect of particle distribution.

- The trap array aspect ratio A_r is defined by the ratio between the number of lines N_l in stream

direction and the number of columns N_c in lateral direction of the trap array:

$$A_r = \frac{N_l}{N_c} \quad (9)$$

This ratio is maybe the less intuitive, but we will see that it may play a role. Most studies show trapping array with an $A_r < 1$ but without motivating this choice. We thus intend to inspect its role.

- And finally, in order to characterize the importance of the channel width occupied by particles at the inlet, we introduce, the inlet and outlet channels to cavity width ratio in the lateral direction:

$$Wch_r = \frac{w_{io}}{W} \quad (10)$$

All the trapping arrays described in the literature have a regular trap distribution in the cavity. We therefore question the role of this regularity and how the results are affected when disorder is introduced into the traps positioning. To do so, we start from a regular trap position structure (Figure 1) and introduce irregularities in the trap network. This is achieved by applying a randomized translation along the horizontal and vertical directions of each trap "i":

$$\begin{cases} x_i = x_{oi} + \psi_x(i) D_f \Delta x \\ y_i = y_{oi} + \psi_y(i) D_f \Delta y \end{cases} \quad (11)$$

where (x_i, y_i) are the coordinates of the i^{th} trap bottom left corner (point M in Figure 1), (x_{oi}, y_{oi}) its original coordinates following the rectangular staggered pattern, ψ_x and ψ_y are independent random distributions of numbers between -1 and 1 , D_f a positive constant called "disorder factor" between 0 and 1 . We have tested two ways of introducing disorder into the lattice, uniform and centered Gaussian with a standard deviation of 0.3 distributions for ψ_x and ψ_y .

2.4 Experimental protocol

The precise microfabrication steps were the same as those for [19] and are very briefly mentioned in this section. A microfluidic chamber resulting from disorder study is fabricated using single layer standard photo-lithography techniques. Based on previous trapping array studies in the literature, we have chosen to connect 4 identical disordered trapping arrays in parallel [14] (Figure 2b,c). A chrome photomask is fabricated by direct laser writing. A circular $h = 14 \mu\text{m}$ thick layer of photoresist resin is generated on a silicon wafer following a spin coating protocol. A master is obtained by UV-light activation and dissolution of the non-activated photoresist resin. PDMS is mold on the master and the microfluidic chip is closed by sticking a glass coverslip on the chip following a plasma activation protocol. The microfluidic chip is then observed using fluorescent microscopy with a 10X magnification (Figure 2d). The inlet and

outlet channels are connected to a pressure controller with a pressure drop Δp corresponding to a flow rate $Q_v = 0.5 \mu\text{l min}^{-1}$ and a $C_p = 10^6 \text{ ml}^{-1}$ concentrated solution of fluorescent particles (Figure 2a), hydraulic resistance variation of the chip is negligible during all the experiment [19].

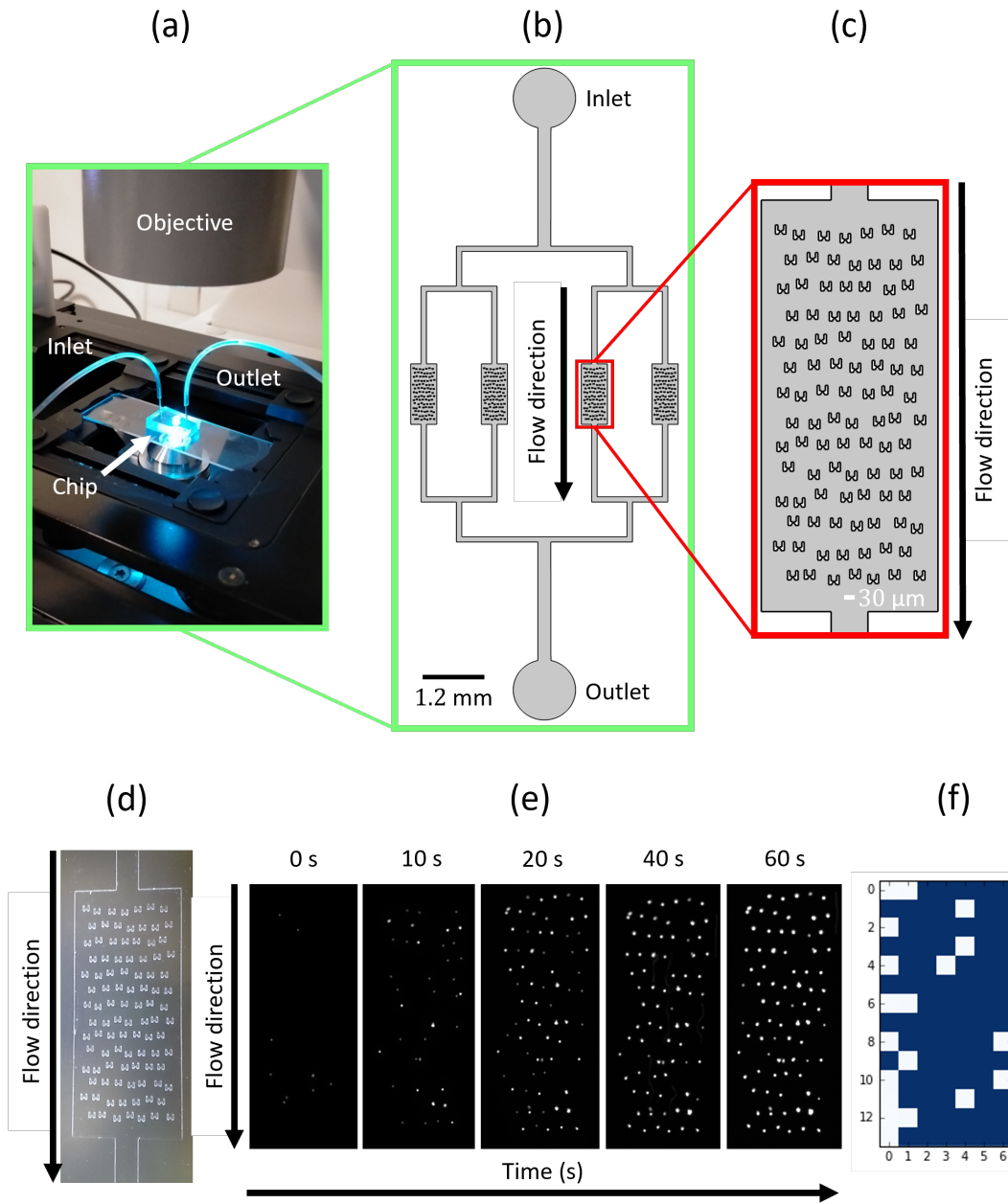


Figure 2: (a) Picture of the experimental setup. The microfluidic chip is connected to a pressure regulator with inlet and outlet tubes. The particle and fluid flow is recorded on the microscope. (b) Scheme of the microfluidic chip constituted by 4 identical trapping arrays connected in parallel. (c) Zoom on one disordered microfluidic trapping array (obtained for $D_f = 0.3$). (d) PDMS fabricated chamber following standard photolithography process observed thanks to a binocular magnifier. (e) Fluorescence microscopy images of the trapping array filling with 5 μm polystyrene bead at different times of the experiment. (f) Binary matrix of the trapping array stationary filling. blue boxes correspond to occupied traps whilst white boxes represent empty traps.

3 Results and discussion

3.1 Parametric study of cavity geometry

We study the influence of the five cavity dimensionless parameters: C , W_r , L_r , A_r , and Wch_r on filling efficiency E_{fill} and capture efficiency E_{capt} as defined in Section 2.3. Each parameter's influence is screened over ten values while keeping the other parameters constant. In Figure 3a, filling and capture efficiencies are shown to be 96% correlated over the 50 simulations conducted. Thus, optimising the trapping array geometry using E_{fill} or E_{capt} as the objective function should yield similar trends and optimal parameter values. Therefore, the study focuses solely on filling efficiency, with capture efficiency results provided in supplementary Figure 9 in Section 9.1. Figure 3b summarizes the evolution of filling efficiency for a regular trapping array, indicating that all cavity parameters influence E_{fill} , with W_r showing an impact of $\pm 20\%$ and A_r $\pm 44\%$. The maximal filling efficiency is obtained for $C = 55.5\%$ (orange point).

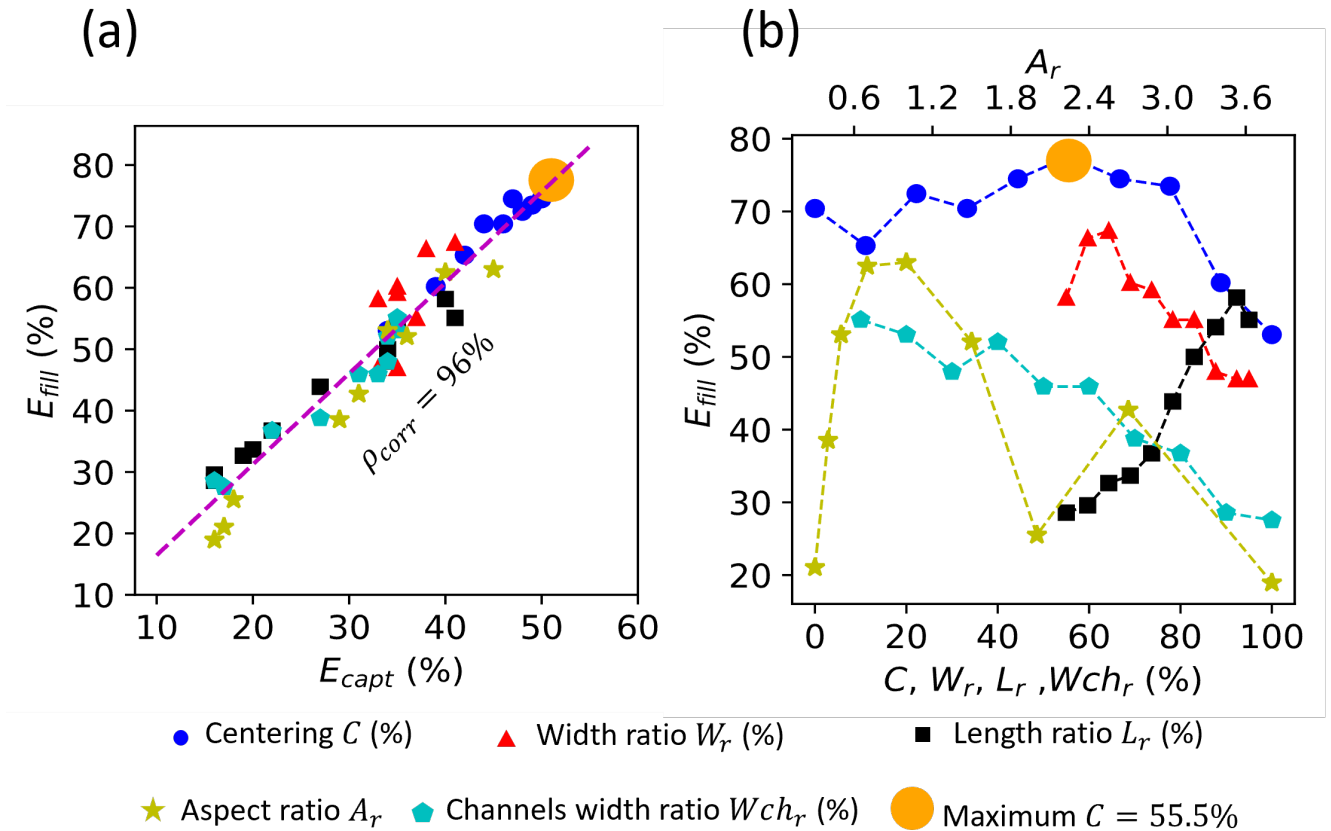


Figure 3: (a) Filling efficiency as a function of capture efficiency for each parametric study, the linear correlation coefficient is $\rho_{corr} = 96\%$. (b) Influence of the five cavity dimensionless parameters C , W_r , L_r , A_r and Wch_r on filling efficiency.

Figure 4a shows the particle trajectories and final positions in the best geometry we get so far (corresponding to the orange point previous Figure 3b). We see that trapped particle trajectories exhibit zigzag-like patterns between traps that are slightly deflected in the lateral direction (from the left to the

right, red trajectories Figure 4a). We previously highlighted the performances of such oblique flow in the case of a maximal inlet/outlet shift ($C = 0\%$) [19], but it seems that an optimum inlet/outlet shift exists for a relative centering C between 44% and 66% (Figure 3b).

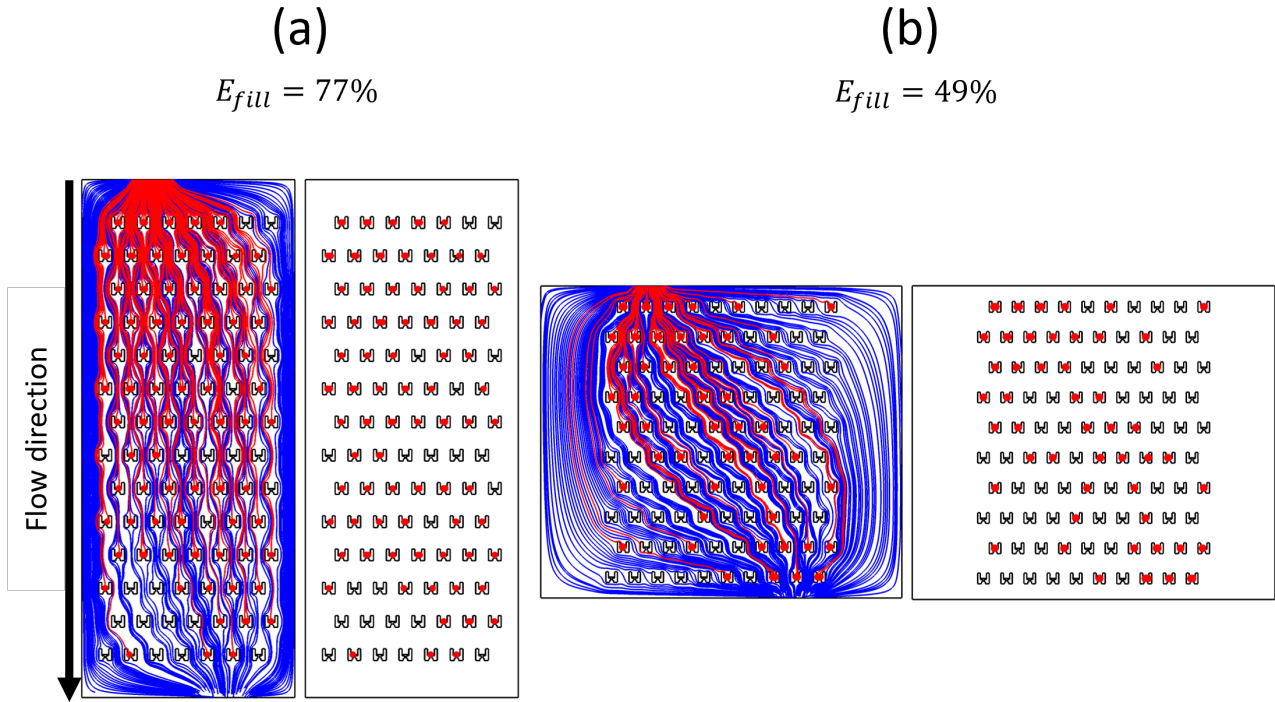


Figure 4: (a) Particle trajectories and final positions for the best geometry resulting from single parametric study. (b) Particle trajectories and final positions for the geometry obtained combining each optimum values from the each parametric study. The corresponding parameter values are: $C = 55.5\%$, $W_r = 64\%$, $L_r = 90\%$, $A_r = 1$ and $Wch_r = 10\%$. The trapped particles and their trajectories are represented in red, the untrapped particle trajectories are represented in blue. The trapped particle diameter is increased to improve readability.

Nonetheless, an optimal inlet/outlet shift is not the same for a different inlet/outlet channel width for example (different Wch_r). Thus, a simple optimisation approach fixing each parameter to its optimal value from this first study can not result in an efficient geometry. Indeed, the geometry built with each optimum values taken separately exhibits a low filling efficiency (49%) with respect to the current optimal one (77%), see Figure 4b. We deduce that optimisation of trapping array-chamber trapping efficiency is a complex and non-intuitive process and is about finding a compromise between combinations of geometric parameters which justifies a multiparametric optimisation approach.

3.2 Optimisation of a regular trap array

This section explores the use of local (Nelder-Mead [26]) and global (Monte Carlo [27]) optimisation techniques in maximizing filling efficiency E_{fill} , as defined in Section 3.2. The optimisation problem consists in finding optimal set of parameter values leading to a maximum of an objective function. For implementation simplicity, we defined the optimisation objective function as capture efficiency:

$E_{capt}(C, W_r, L_r, A_r, Wch_r)$. The optimisation results should also be optimal in filling efficiency due to the strong correlation between both metrics. Figure 5a illustrates the local optimisation technique for a single variable objective function (blue curve) having two maxima: M_1 and M_2 points. M_1 is a local but not global maximum of the objective function whilst M_2 is the global maximum of the objective function. First, an initial set of parameter value is chosen and the objective is calculated: I_1, I_2, I_3 and I_4 represent 4 different choices of initial values. A local optimisation algorithm follows the fastest growth of the objective function from the chosen initial point with or without calculating the derivative(s) of the objective function like a blinded walker trying to reach a peak of a mountain chain [28]. Since we have no proof of E_{capt} differentiability with respect to the parameters, we choose a derivative-free method: the simplex-based Nelder-Mead method. Depending on the initial parameter values, the local optimisation algorithm converges towards different maxima: from the I_1 and I_2 points, the convergence point is M_1 whilst from the I_3 and I_4 points, the convergence point is M_2 . The main advantage of local optimisation is the low number of model evaluations needed to find an optimum. However, it can stick into local maxima and miss the global maximum.

All the different local optimisations we tried converge towards different local maxima. Thus, we used a global optimisation algorithm (Monte Carlo) which can not stick into local maxima. This technique randomly samples points within a uniform distribution inside the domain of parameters variations specified by us [28]. The convergence of such algorithm is low and not guaranteed. However, since the model has a low computational cost, this method seems appropriate and we limit the number of model evaluation to 2000 for approximately 1 day of computation time. As expected, we obtain our best filling efficiency with this algorithm: $E_{fill} = 81\%$, which is 4% better than the best geometry obtained by the parametric study (with $E_{fill} = 77\%$).

Figure 5b shows the particle trajectories and final positions for the globally optimised geometry. The corresponding parameter values are: $C = 44\%$, $W_r = 78\%$, $L_r = 87\%$, $A_r = 50\%$, $Wch_r = 48\%$. Interestingly, it seems difficult to reach a filling efficiency better than about 81%. In addition, the fact that $C \neq 100\%$ confirms the importance of an oblique flow that allows increasing filling efficiency. We believe that the symmetry breaking between the upstream and downstream flow allows a lateral dispersion of the particles. As such, mass transport in the lateral direction of the flow should be improved by adding disorder in the design of the trapping array which is the subject of the next section.

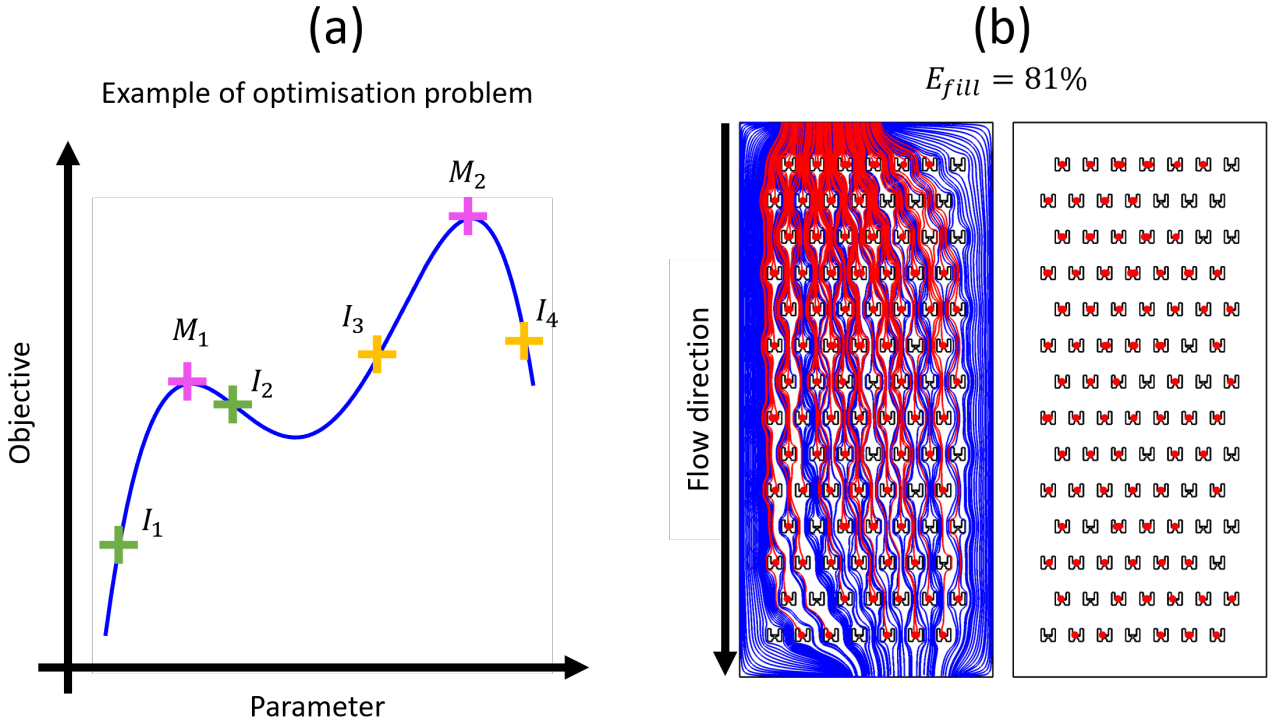


Figure 5: (a) Sketch of the local optimisation principle for a single parameter objective function. M_1 and M_2 are maximums of the function. I_1, I_2, I_3 and I_4 points represent 4 different choices of initial values. (b) Particle trajectories and final positions in the globally optimised chamber. The trapped particles and their trajectories are represented in red, the untrapped particle trajectories are represented in blue. The trapped particle diameter is increased to improve readability.

3.3 Improving filling efficiency using disorder

Although the numerical model has been validated previously [19], we conducted a preliminary experimental verification to assess the efficiency of a disordered trapping array. This experiment utilizes $5 \mu\text{m}$ diameter fluorescent polystyrene beads within a uniformly disordered array with a disorder factor of $D_f = 0.3$. Under controlled flow conditions of $0.5 \mu\text{l min}^{-1}$, a steady-state filling is attained within 60 s, yielding a filling efficiency of 81% (Figure 2e,f). This efficiency markedly surpasses the typical 50% filling observed in symmetric chambers [19]. This result highlights the impact of disorder on filling efficiency, motivating further exploration through detailed numerical simulations.

Therefore, we now investigate how the addition of disorder on the trap positioning may affect filling efficiency by numerical simulations. For this purpose, we explore geometries generated as described in section 2.3. The initial geometry is the reference geometry (shown Figure 1) of low filling efficiency ($E_{fill} = 51\%$). Disorder is then added in the trapping array using 10 different values of the disorder factor D_f introduced in section 2.3. As the trapping array geometry is built with probability laws, the repeatability of the results is assessed by rebuilding the geometry 10 times for each D_f value. Figure 6 shows the evolution of E_{fill} with respect to the disorder factor D_f for uniform (a) and Gaussian (b) disorders. We notice that for a same D_f value (same colour), a variety of different geometries can be

obtained, leading to a dispersity of filling efficiency about 15% (bounded by the maximum and minimum values). For both disorder distributions, we observe that the mean filling efficiency increases with the disorder parameter and reach a plateau about $\sim 72\%$ (black crosses) at $D_f \geq 0.3$ for the uniform and at $D_f \geq 0.5$ for the Gaussian disorder. For both disorder distributions, a maximum of filling efficiency is identified to be of 80% (pink stars) which is very close to the previous one of 81% obtained for the optimisation of a regular trapping array. The best geometries are respectively obtained for $D_f = 0.40$ and $D_f = 0.64$ for uniform and Gaussian distributions respectively. Therefore, uniform and Gaussian disorders are equally efficient and can reach very similar efficiencies as an optimised oblique chamber with a staggered trap array.

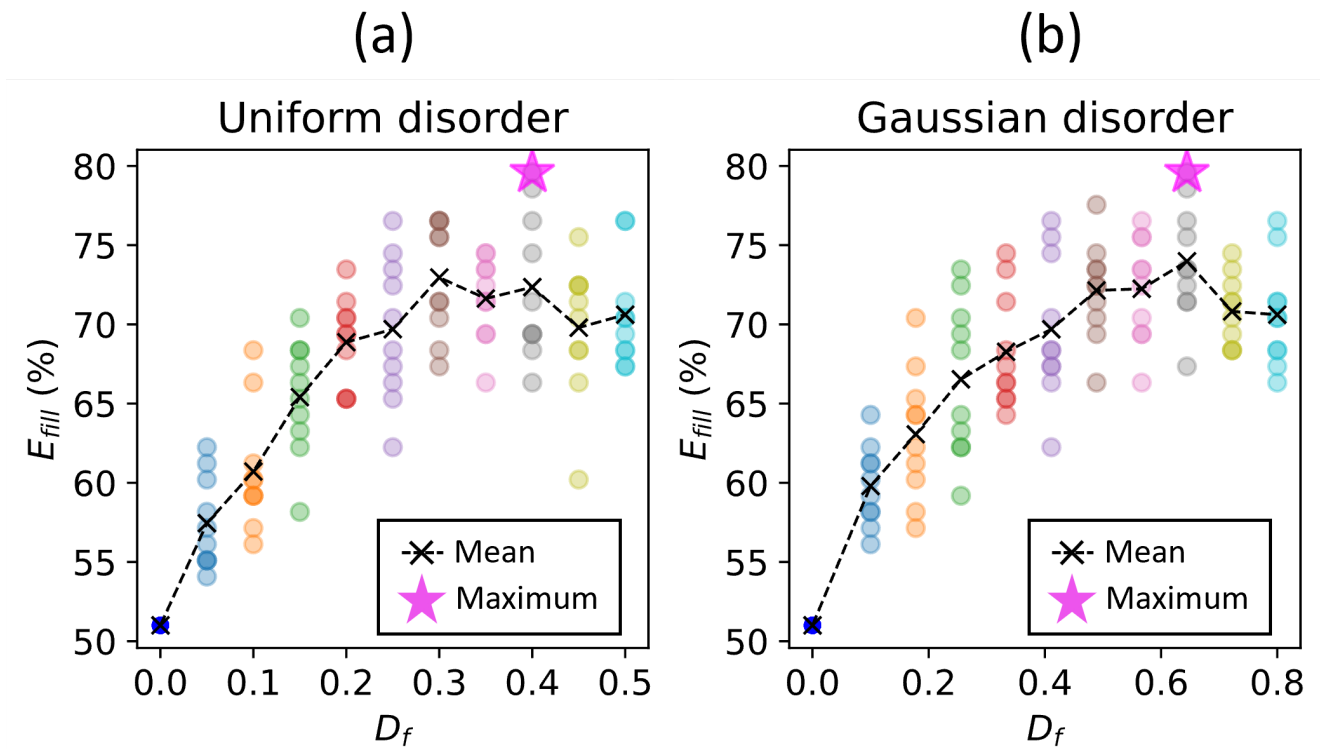


Figure 6: Evolution of filling efficiency in a disordered trapping array with a symmetric cavity (same cavity as in Figure 1) with respect to a uniform (a) and a Gaussian distribution (b) of the disorder factor D_f . Each simulation is represented by a dot. For each D_f value, the geometry is re-built 10 times, which corresponds to a fixed colour of vertically aligned dots. Dot colour appears darker when several point overlaps *i.e* when several simulation results are equal in filling efficiency for a same D_f value. Black crosses represent the mean of E_{fill} values for each D_f value. Black crosses are connected by dashed lines to improve visibility.

Figure 7 shows the particle trajectories and final positions for the symmetric reference chamber (a), the best uniform (b) and best Gaussian (c) distributions of the disorder factor. The respective filling efficiencies are 51% (reference geometry) and 80% for both uniform and Gaussian disorders (corresponding to the big pink stars Figure 6a,b).

In a symmetric chamber where inlet and outlet channels are perfectly aligned, streamlines exhibit upstream/downstream symmetry along the traps far enough from the inlet and outlet (Figure 7a). There-

fore, the first trap rows are filled by the particles in the flow direction and almost all the next trap rows stay empty. Then, non-trapped particles display zigzag-like trajectories around the traps, see zoom of Figure 7a. Breaking the upstream/downstream flow symmetry thanks to the addition of disorder modify the symmetric streamline patterns and allows a spanwise mass transport up to eventually filling a next trap. For optimised oblique trapping arrays, this spanwise mass transport is provided by the shift between the inlet and the outlet channels. A symmetry breaking of upstream/downstream streamlines in disordered trapping array is also clearly visible in the zooms of Figure 7b and 7c. Indeed, a saddle point appears on the upstream side of the trap, and streamlines recombine downstream. By breaking the symmetry, streamlines may explore traps in the lateral direction, a possibility that would not have been possible with a staggered trap array. Therefore, we think that lateral dispersion is a key mechanism allowing flow symmetry breaking and then particle trapping. Such mechanism should be quantitatively investigated which is the subject of the next section.

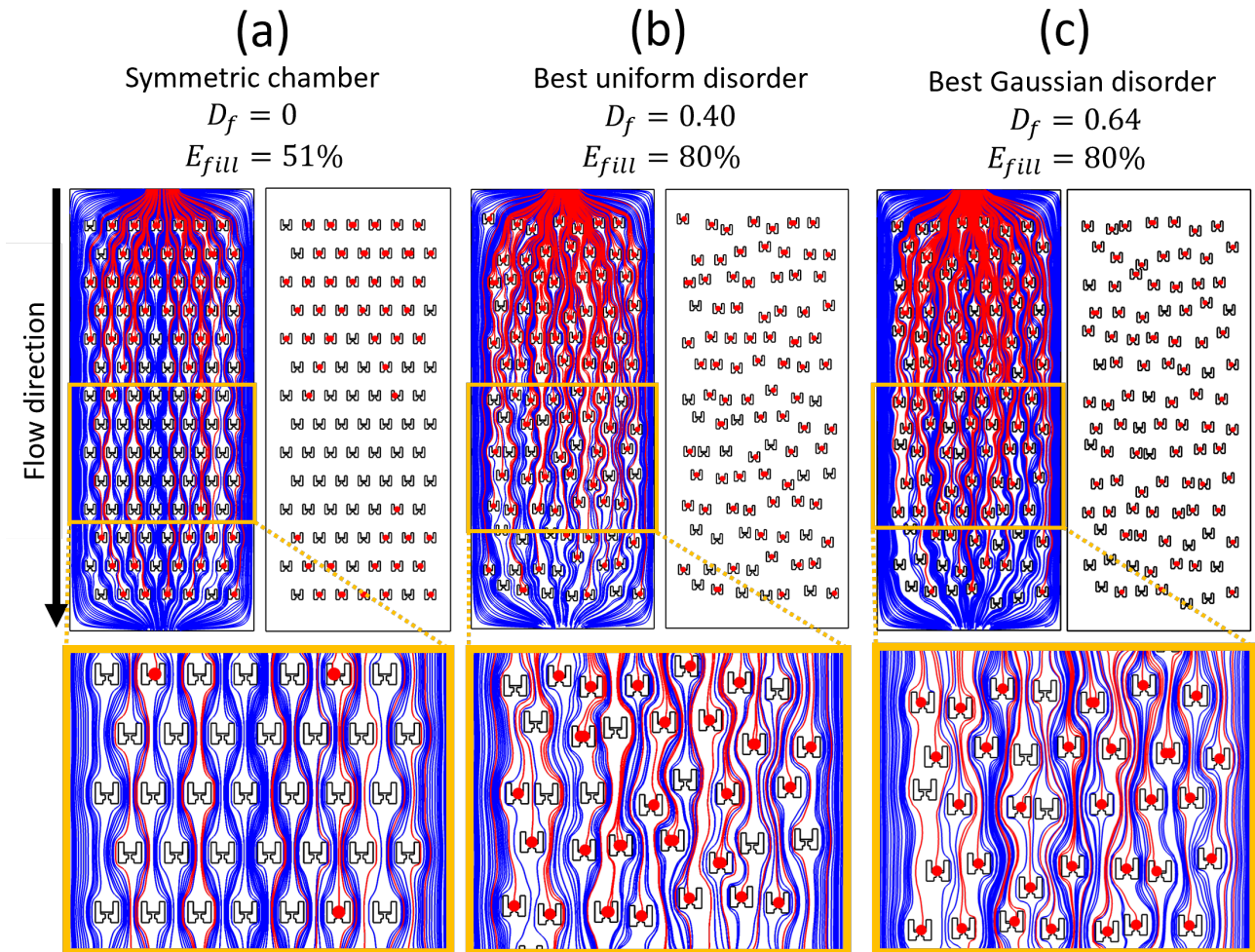


Figure 7: Particle trajectories and final positions in a symmetric chamber (a), the disordered chamber for the best uniform (b) and Gaussian (c) distributions. The trapped particles and their trajectories are represented in red, the untrapped particle trajectories are represented in blue. The trapped particle diameter is increased to improve readability.

Before this quantitative analysis, we would like to point a remark: the significant increase of filling

efficiency is not observed when adding disorder to the optimised oblique cavity presented in previous section (see supplementary section 9.2). In this case, filling efficiency stagnates in average and the best filling efficiency is 78% (see supplementary Figure 10a), which is close to the best filling efficiencies obtained so far of 80%, Figure 7b). Therefore, we think that uniform disorder allows to maintain approximately 80% of filling efficiency independently of the cavity geometry. We can take advantage of this independence to increase the size of the trap array in the lateral direction at will (see supplementary section 9.2.1).

3.4 How lateral dispersion influences trapping efficiency

Particle pair dispersion in the lateral direction is quantified by the lateral distance between two particles $d_{\perp}(t) = y_2(t) - y_1(t)$ where $y_1(t)$ and $y_2(t)$ are the lateral coordinates of two initially close particles. At the whole population scale, lateral pair dispersion is characterized by the mean-square lateral distance $\langle d_{\perp}^2(t) \rangle$ and the mean-square deviation $\sigma_{\perp}^2(t) = \langle (d_{\perp}(t) - \langle d_{\perp} \rangle(t))^2 \rangle = \langle d_{\perp}^2(t) \rangle - \langle d_{\perp}(t) \rangle^2$ of the lateral particle pair distance $d_{\perp}(t)$.

Figure 8a presents the time variations of $\langle d_{\perp}^2 \rangle(t)$ on a \log_{10} - \log_{10} scale. In diffusive transport, particle pair distance scales proportionally with time: $\langle d_{\perp}^2 \rangle(t) \propto t$, exhibiting a unitary slope (pink dashed line) in Figure 8a. In microfluidic trapping arrays, advection dominates over diffusion, resulting in a sub-diffusive dispersion regime (see Figure 8a) characteristic of microfluidic flows in porous media [29]. The trends in Figure 8a indicate two distinct phases for all trapping array geometries: an initial quasi-linear growth with a slope slightly below that of diffusion and a subsequent slowdown phase. For the symmetric chamber, the linear phase is brief (blue curve) and transitions rapidly to the slowdown phase (blue curve after $\log_{10}t = 0$ s). In contrast, for the disordered and optimised oblique chambers, the linear regime persists longer (red and green curves until $\log_{10}t \approx 0.3$ s), leading to faster lateral dispersion.

Figure 8b displays the time evolution of the lateral mean-square deviation $\sigma_{\perp}^2(t)$. Interestingly, it seems to reach an asymptotic value for the symmetric chamber at the larger times (blue curve) while the values continue to increase for the disordered and oblique chambers (red and green curves). Moreover, we still note a brief quasi-linear growth of $\sigma_{\perp}^2(t)$ ending at $t = 1$ s (*i.e.* $\log_{10}t = 0$ s Figure 8a). For the disordered and optimised oblique chambers, this phase extends to $t = 2$ s, (*i.e.* at $\log_{10}t = 0.3$ s Figure 8a) which results in a $\sigma_{\perp}^2(t)$ twice larger than for the symmetric chamber. The trends and values of $\sigma_{\perp}^2(t)$ are similar for the disordered and optimised oblique chambers.

These observations confirm the hypothesis that lateral dispersion plays a critical role in improving filling efficiency. While the optimised oblique and disordered chambers achieve lateral dispersion through different mechanisms, their dispersion regimes are similar, which explains their comparable filling efficiencies ($\approx 80\%$). In contrast, the symmetric chamber, with significantly lower lateral dispersion, exhibits poorer filling efficiency, ($\approx 50\%$).

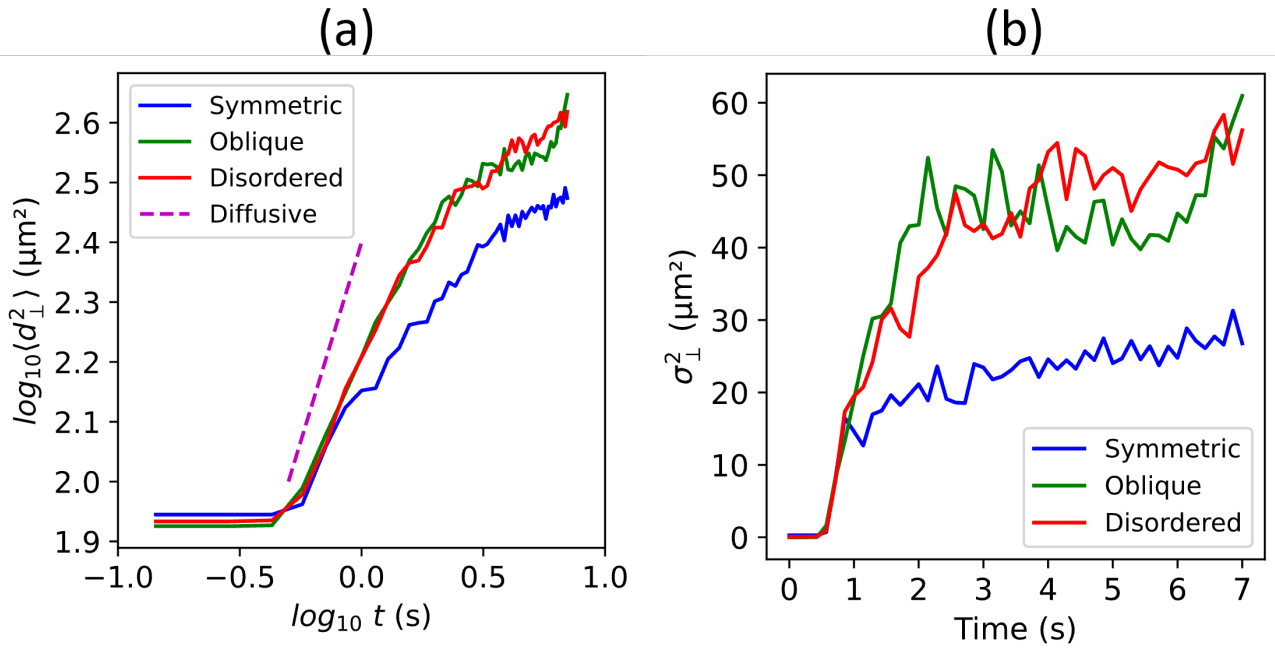


Figure 8: Statistics of lateral dispersion in the three chambers: symmetric, oblique and disordered. (a) Logarithm of the mean square lateral distance $\langle d_{\perp}^2 \rangle$ as a function of the logarithm of time t . The "Diffusive" line has a unitary slope and (b) Mean-square deviation σ_{\perp}^2 of the lateral distance d_{\perp} between particles as a function of time t .

4 Conclusion

In this study, we investigate the trapping efficiency of dense single layer trapping arrays. We adapt our previously validated CFD/particle model to parametrically optimise the filling efficiency with five dimensionless geometric parameters. After confirming that each parameter influences the capture and filling efficiencies, we use different algorithmic optimisation approaches (local and global) on a regular trapping array. The results show the importance of creating an oblique flow to increase filling efficiency. These oblique flows break the upstream/downstream flow symmetry around the traps and thus enhance lateral dispersion of the particles favouring particle exploration over a wider area. While improving lateral dispersion is a critical point in favouring trap filling, we show that similar filling efficiencies can be obtained by introducing disorder into the trap paving. An advantage of this configuration is that it does not constrain the cavity and inlet/outlet geometry for similar filling efficiencies than an optimised oblique flow geometry. Finally, a quantitative study of lateral dispersion in the optimised oblique, disordered and symmetric geometries reveals the link between the lateral dispersion of particles and trapping array filling efficiency. We think that further experimental investigations on very large trapping arrays should finally reveal which geometry is the most interesting.

5 Acknowledgements

This work has received support from the administrative and technological staff of “Institut Pierre-Gilles de Gennes” (Laboratoire d’excellence : ANR-10-LABX-0031, “Investissements d’avenir” : ANR-10-IDEX-0001-02 PSL and Equipement d’excellence : ANR-10-EQPX-0034). NR acknowledges funding from the École Normale Supérieure de Rennes (ENS Rennes, Contrat Doctoral Spécifique Normalien) for PhD scholarship. MCJ acknowledges CNRS and Université de Rennes for financial support.

6 Author contributions

Concepts were proposed by MCJ and JF. Data curation was done by NR and formal analysis by MCJ and NR. Simulations were performed by NR, experiments were conducted by GF (fabrication, trapping) and NR (trapping). NR, MCJ and JF built the methodology and interpreted the results. The manuscript was written by NR and reviewed for scientific and technical aspects by MCJ and JF and for formal aspects by MCJ and RA. Work was supervised by MCJ, JF and RA. Access to simulation material was supported by RA.

7 Conflicts of interest

There are no conflicts of interest to declare.

References

- [1] Mirren Charnley, Marcus Textor, Ali Khademhosseini, and Matthias P. Lutolf. Integration column: Microwell arrays for mammalian cell culture. Integrative Biology, 1(11-12):625–634, 2009. ISSN 17579694. doi: 10.1039/b918172p.
- [2] Etienne Fradet, Craig McDougall, Paul Abbyad, Rémi Dangla, David McGloin, and Charles N. Baroud. Combining rails and anchors with laser forcing for selective manipulation within 2D droplet arrays. Lab on a Chip, 11(24):4228–4234, 2011. ISSN 14730189. doi: 10.1039/c1lc20541b.
- [3] Xavier A. Figueroa, Gregory A. Cooksey, Scott V. Votaw, Lisa F. Horowitz, and Albert Folch. Large-scale investigation of the olfactory receptor space using a microfluidic microwell array. Lab on a Chip, 10:1120–1127, 2010. ISSN 14730189. doi: 10.1039/b920585c.
- [4] Nassim Rousset, Frédéric Monet, and Thomas Gervais. Simulation-assisted design of microfluidic sample traps for optimal trapping and culture of non-adherent single cells, tissues, and spheroids. Scientific Reports, 7(1):1–12, 2017. ISSN 20452322. doi: 10.1038/s41598-017-00229-1.
- [5] Adam Winkleman, Katherine L. Gudiksen, Declan Ryan, George M. Whitesides, Derek Greenfield, and Mara Prentiss. A magnetic trap for living cells suspended in a paramagnetic buffer. Applied Physics Letters, 85:2411–2413, 9 2004. ISSN 00036951. doi: 10.1063/1.1794372.
- [6] Kristian Smistrup, Torsten Lund-Olesen, Mikkel F. Hansen, and Peter T. Tang. Microfluidic magnetic separator using an array of soft magnetic elements. Journal of Applied Physics, 99, 2006. ISSN 00218979. doi: 10.1063/1.2159418.
- [7] Ying Zhou, Srinjan Basu, Kai J. Wohlfahrt, Steven F. Lee, David Klenerman, Ernest D. Laue, and Ashwin A. Seshia. A microfluidic platform for trapping, releasing and super-resolution imaging of single cells. Sensors and Actuators, B: Chemical, 232:680–691, 2016. ISSN 09254005. doi: 10.1016/j.snb.2016.03.131.
- [8] Anthony K. Au, Hoyin Lai, Ben R. Utela, and Albert Folch. Microvalves and micropumps for BioMEMS, volume 2. Molecular Diversity Preservation International (MDPI), 2011. ISBN 1206616903. doi: 10.3390/mi2020179.
- [9] A. N. Grigorenko, N. W. Roberts, M. R. Dickinson, and Y. Zhang. Nanometric optical tweezers based on nanostructured substrates. Nature Photonics, 2:365–370, 6 2008. ISSN 17494885. doi: 10.1038/nphoton.2008.78.

- [10] Adam Rosenthal and Joel Voldman. Dielectrophoretic traps for single-particle patterning. Biophysical Journal, 88:2193–2205, 2005. ISSN 00063495. doi: 10.1529/biophysj.104.049684.
- [11] Lylian Challier, Justin Lemarchand, Catherine Deanno, Cecile Jauzein, Giorgio Mattana, Guillaume Mériguet, Benjamin Rotenberg, and Vincent Noël. Printed dielectrophoretic electrode-based continuous flow microfluidic systems for particles 3d-trapping. Particle and Particle Systems Characterization, 38, 2 2021. ISSN 15214117. doi: 10.1002/ppsc.202000235.
- [12] H. Lee, A. M. Purdon, and R. M. Westervelt. Manipulation of biological cells using a micro-electromagnet matrix. Applied Physics Letters, 85:1063–1065, 8 2004. ISSN 00036951. doi: 10.1063/1.1776339.
- [13] Mikael Evander, Linda Johansson, Tobias Lilliehorn, Jure Piskur, Magnus Lindvall, Stefan Johansson, Monica Almqvist, Thomas Laurell, and Johan Nilsson. Noninvasive acoustic cell trapping in a microfluidic perfusion system for online bioassays. Analytical Chemistry, 79:2984–2991, 4 2007. ISSN 00032700. doi: 10.1021/ac061576v.
- [14] Alison M. Skelley, Oktay Kirak, Heikyung Suh, Rudolf Jaenisch, and Joel Voldman. Microfluidic control of cell pairing and fusion. Nature Methods, 6(2):147–152, 2009. ISSN 15487091. doi: 10.1038/nmeth.1290.
- [15] Léa Pinon, Nicolas Ruysen, Judith Pineau, Olivier Mesdjian, Damien Cuvelier, Anna Chipont, Rachele Allena, Coralie L. Guerin, Sophie Asnacios, Atef Asnacios, Paolo Pierobon, and Jacques Fattaccioli. Phenotyping polarization dynamics of immune cells using a lipid droplet-cell pairing microfluidic platform. Cell Reports Methods, page 100335, 2022. ISSN 26672375. doi: 10.1016/j.crmeth.2022.100335.
- [16] Judith Pineau, Léa Pinon, Olivier Mesdjian, Jacques Fattaccioli, Ana-Maria Lennon-Duménil, and Paolo Pierobon. Microtubules restrict F-actin polymerization to the immune synapse via GEF-H1 to maintain polarity in lymphocytes. Elife, 11, 2022. doi: 10.7554/elife.78330.
- [17] Donald Wlodkowic, Shannon Faley, Michele Zagnoni, John P. Wikswow, and Jonathan M. Cooper. Microfluidic single-cell array cytometry for the analysis of tumor apoptosis. Analytical Chemistry, 81(13):5517–5523, 2009. ISSN 00032700. doi: 10.1021/ac9008463.
- [18] Dino Di Carlo, Nima Aghdam, and Luke P. Lee. Single-cell enzyme concentrations, kinetics, and inhibition analysis using high-density hydrodynamic cell isolation arrays. Analytical Chemistry, 78(14):4925–4930, 2006. ISSN 00032700. doi: 10.1021/ac060541s.
- [19] O. Mesdjian, N. Ruysen, M. C. Jullien, R. Allena, and J. Fattaccioli. Enhancing the capture efficiency and homogeneity of single-layer flow-through trapping microfluidic devices using oblique

- hydrodynamic streams. Microfluid. Nanofluidics, 25(11):1–11, 2021. ISSN 16134990. doi: 10.1007/s10404-021-02492-1.
- [20] Stefan Kobel, Ana Valero, Jonas Latt, Philippe Renaud, and Matthias Lutolf. Optimization of microfluidic single cell trapping for long-term on-chip culture. Lab on a Chip, 10(7):857–863, 2010. ISSN 14730189. doi: 10.1039/b918055a.
- [21] Ahmad Sohrabi Kashani and Muthukumaran Packirisamy. Efficient Low Shear Flow-based Trapping of Biological Entities. Scientific Reports, 9(1):1–15, 2019. ISSN 20452322. doi: 10.1038/s41598-019-41938-z.
- [22] Donald Wlodkowic and Jonathan M. Cooper. Microfluidic cell arrays in tumor analysis: New prospects for integrated cytomics. Expert Review of Molecular Diagnostics, 10(4):521–530, 2010. ISSN 14737159. doi: 10.1586/erm.10.28.
- [23] Xiaoxiao Xu, Zhenyu Li, and Arye Nehorai. Finite element simulations of hydrodynamic trapping in microfluidic particle-trap array systems. Biomicrofluidics, 7(5), 2013. ISSN 19321058. doi: 10.1063/1.4822030.
- [24] Yeye Xu, Weiping Ding, Shibo Li, Chengpan Li, Dayong Gao, and Bensheng Qiu. A single-cell identification and capture chip for automatically and rapidly determining hydraulic permeability of cells. Analytical and Bioanalytical Chemistry, 412(19):4537–4548, 2020. ISSN 16182650. doi: 10.1007/s00216-020-02704-7.
- [25] Donatien Mottin, Florence Razan, Frédéric Kanoufi, and Marie-Caroline Jullien. Influence of lift forces on particle capture on a functionalized surface. Microfluid. Nanofluid., 25(11):1–10, November 2021. ISSN 1613-4990. doi: 10.1007/s10404-021-02488-x.
- [26] J. A. Nelder and R. Mead. A simplex method for function minimization. The Computer Journal, 7(4):308–313, 01 1965. ISSN 0010-4620. doi: 10.1093/comjnl/7.4.308.
- [27] Comsol Multiphysics. Optimization module user’s guide. Optimization module User’s guide, Optimization module User’s guide:78, 2018.
- [28] Gerhard Venter. Review of Optimization Techniques, chapter 2,3, pages 1–10. John Wiley and Sons, Ltd, 2010. ISBN 9780470686652. doi: <https://doi.org/10.1002/9780470686652.eae495>.
- [29] Pietro de Anna, Tanguy Le Borgne, Marco Dentz, Alexandre M. Tartakovsky, Diogo Bolster, and Philippe Davy. Flow intermittency, dispersion, and correlated continuous time random walks in porous media. Phys. Rev. Lett., 110:184502, May 2013. doi: 10.1103/PhysRevLett.110.184502. URL <https://link.aps.org/doi/10.1103/PhysRevLett.110.184502>.

8 Supplementary information to: Materials and Method

8.1 Model parameters values

The numerical parameters used in the model are reported in the following Table 1.

Fixed geometric parameters	Description	Value
h	chamber's out-of-plane depth	14 μm
w_o	Traps small opening width	4 μm
w_{pil}	Trap pillar width	7 μm
w_{sr}	Traps small rectangle width	10 μm
w_{trap}	Traps width	30 μm
Δx	Horizontal distance between traps	50 μm
Δy	Vertical distance between traps	30 μm
l_{sr}	Trap small rectangle's length	5 μm
l_{trap}	Trap's length	27 μm
N_{traps}	Number of traps in the MTA	96 – 98

Physical parameters	Description	Values
μ	Fluid dynamic viscosity	0.001 Pa s
N_{part}	Number of particles	2 N_{traps}
p_{in}	Uniform inlet pressure	100 Pa
p_{out}	Uniform outlet pressure	0 Pa
ρ	Fluid density	1000 kg m ⁻³
R_p	Particles radius	2.5 μm
T_e	Study time	3 s - 32 s

Parametric & optimisation studies	Description	Values
C	Inlet/outlet centering	[0, 100] %
W_r	Width ratio	[55, 95] %
L_r	Length ratio	[55, 95] %
A_r	Aspect ratio	0.3,0.4,0.5,0.7,1,1.5,2,2.7,3.8
Wch_r	Channel to chamber width ratio	[10, 100] %

Table 1: The model parameters. For single parametric studies, 10 parameters values are chosen to uniformly vary in the specified interval excepted for the A_r parameter where 9 values are chosen to have the same total number of traps ± 3 traps.

8.2 Finite-Element implementation

In COMSOL, the Brinkman equation is written in the classical Continuum Mechanics formulation:

$$\begin{cases} \nabla \cdot \underline{\underline{\sigma}} + \underline{\underline{f}} = \underline{\underline{0}} \\ \nabla \cdot \underline{\underline{v}} = 0 \\ \underline{\underline{\sigma}} = -p\underline{\underline{I}} + 2\mu\underline{\underline{D}} \\ \underline{\underline{D}} = \frac{1}{2} (\nabla \underline{\underline{v}} + (\nabla \underline{\underline{v}})^T) \end{cases} \quad (12)$$

where $\underline{\underline{\sigma}}$ is the Newtonian fluid Cauchy stress tensor, $\underline{\underline{I}}$ the identity tensor and $\underline{\underline{D}}$ the strain rate tensor. The mixed weak form equation implemented in COMSOL is obtained by applying the scalar product of Brinkman equation with test velocity $\hat{\underline{\underline{v}}}$ and by multiplying the mass-conservation (continuity) equation by test pressure \hat{p} and then integration on the fluid domain Ω (grey domain Figure 1):

$$\begin{cases} \int_{\Omega} (\nabla \cdot \underline{\underline{\sigma}}) \cdot \hat{\underline{\underline{v}}} d\Omega + \int_{\Omega} \underline{\underline{f}} \cdot \hat{\underline{\underline{v}}} d\Omega = 0 \\ \int_{\Omega} \hat{p} \nabla \cdot \underline{\underline{v}} d\Omega = 0 \end{cases} \quad (13)$$

Then by integration by part of the first integral and application of the divergence theorem, the following weak form is implemented into COMSOL:

$$\begin{cases} \int_{\Omega} -\underline{\underline{\sigma}} : \nabla \hat{\underline{\underline{v}}} d\Omega + \oint_{\partial\Omega} (\underline{\underline{\sigma}} \cdot \underline{\underline{n}}) \cdot \hat{\underline{\underline{v}}} d\Gamma + \int_{\Omega} \underline{\underline{f}} \cdot \hat{\underline{\underline{v}}} d\Omega = 0 \\ \int_{\Omega} \hat{p} \nabla \cdot \underline{\underline{v}} d\Omega = 0 \end{cases} \quad (14)$$

Where the first integral represents the virtual power of internal forces including viscous and pressure forces. This equation can be implemented into any open-source FEM code such as Freefem++ or Fenics. The second term represents the virtual power of boundary external forces not null only on the inlet and outlet boundaries where the pressure is prescribed and where $\hat{\underline{\underline{v}}}$ is not null. The last term represents the virtual power of external body forces. The latter equations are discretised in space by applying the Finite-Element Method (FEM) with linear Lagrange shape functions for both pressure and velocity fields (P1/P1 elements). Even without advection term, such elements must be stabilised to satisfy Ladyzhenskaya–Babuška–Brezzi (LBB) condition. To do so, the COMSOL consistent streamline stabilisation term is added. The weak form equation discretisation is obtained first by applying the nodal (Galerkin) interpolation for $\underline{\underline{v}}$ and p by their respective interpolation functions and then by replacing the test functions by all interpolation functions. The resulting linear system of equations is numerically inverted using the COMSOL MUMPS solver.

9 Supplementary information to: Results

9.1 Cavity comprehensive parametric study: capture efficiency results

The results of the cavity comprehensive parametric study in capture efficiency (*ie* the proportion of trapped particles defined 2.3) are summarised Figure 9. We notice the very similar curve trends with respect to filling efficiency displayed Figure 3, leading to a 96% linear correlation coefficient between the two metrics (capture and filling efficiencies). As a consequence, the optimum geometry for both metrics is obtained for the same parameter value $C = 55.5\%$.

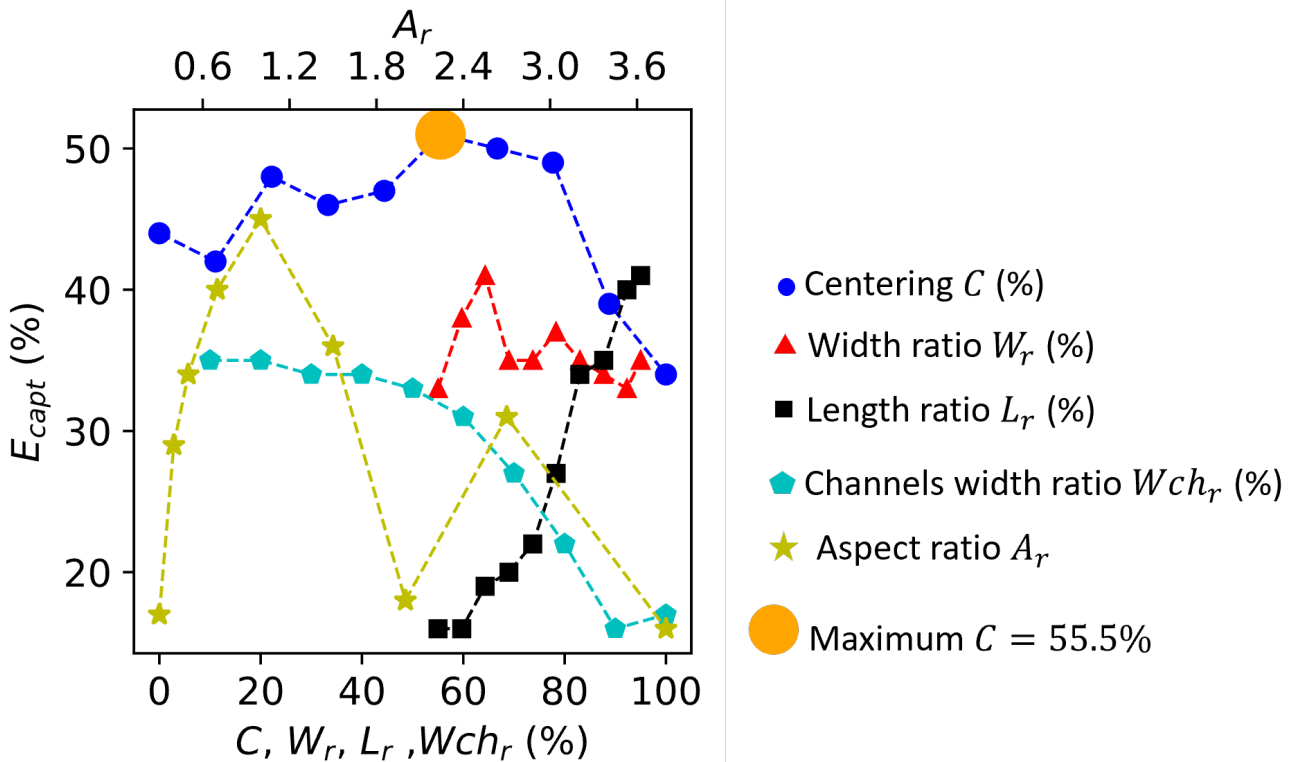


Figure 9: Influence of the five cavity dimensionless parameters C , W_r , L_r , A_r and Wch_r on capture efficiency. When parameters are fixed, their respective values are : $C = 100\%$, $W_r = 84\%$, $L_r = 86\%$, $A_r = 50\%$ and $Wch_r = 23\%$ which corresponds to the reference geometry Figure 1. Results from a same parametric study are connected by dashed lines to improve readability.

9.2 Disorder parametric study for optimised cavity

We study the influence of uniform disorder with the optimised oblique cavity presented section 3.2 and Figure 5b. To do so, we conduct the same disorder factor D_f parametric study as in section 3.3: we screen 10 values of D_f with a geometry rebuilt 10 times for each D_f value. Figure 10(a) shows the evolution of filling efficiency with respect to the disorder factor D_f . Interestingly, adding disorder slightly decreases filling efficiency because the maximum filling efficiency is obtained without adding disorder: $E_{fill} = 81\%$ and the best filling efficiency obtained with a disordered MTA is $E_{fill} = 78\%$ (highest dot for $D_f = 0.5$ Figure 10(a)). Therefore, the use of disordered trap array seems relevant only with a

non-optimised cavity.

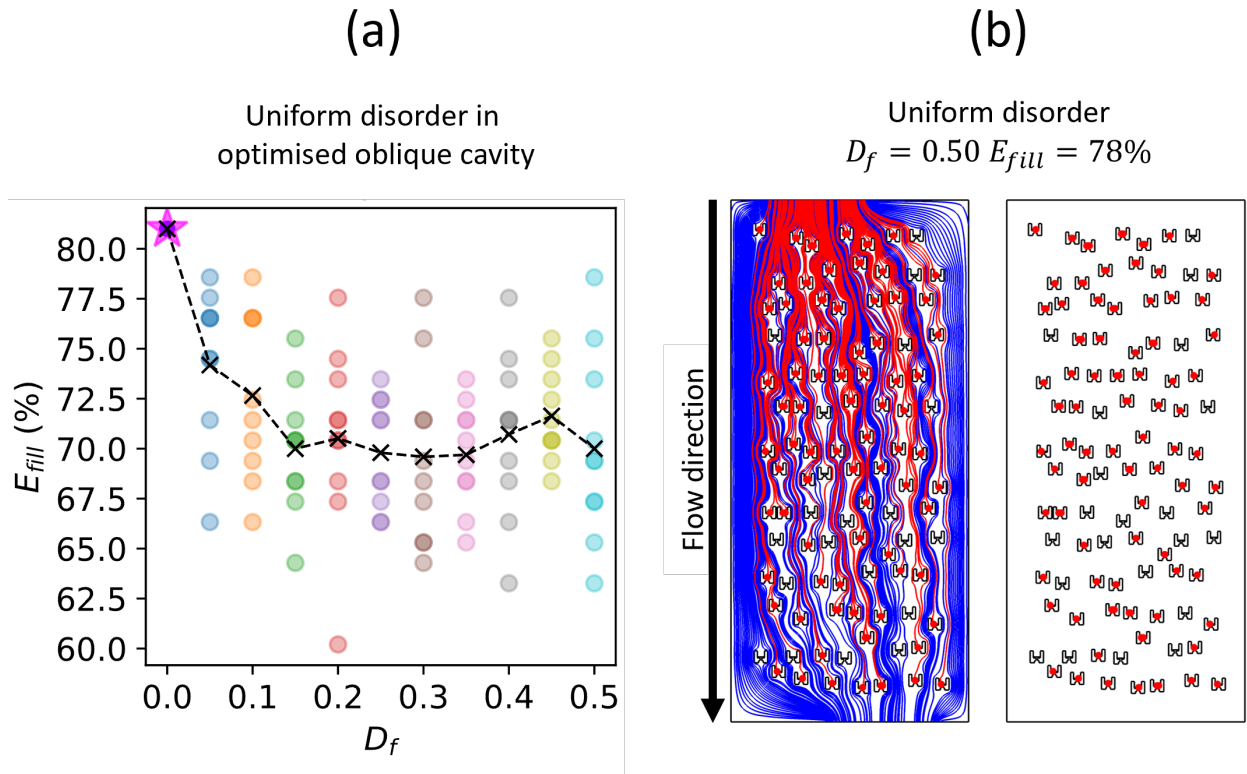
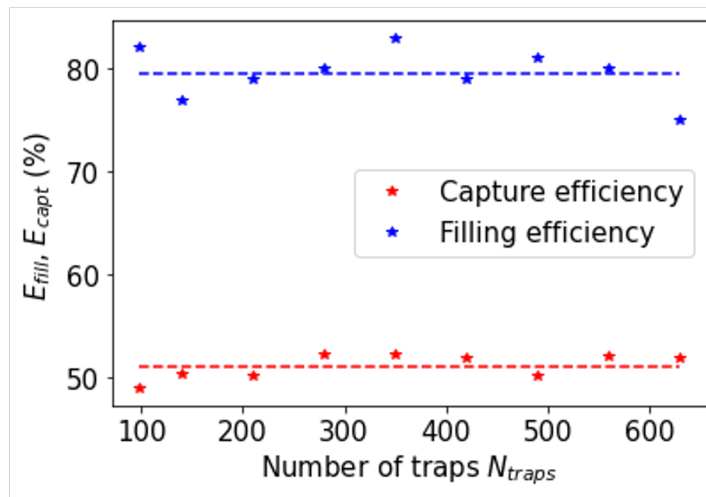


Figure 10: (a) Evolution of capture efficiency with respect to the the disorder factor D_f for a uniform disorder. Each simulation is represented by a dot. For each D_f value, the geometry is re-built 10 times, which corresponds to a fixed colour of vertically aligned dots. Dot colour appears darker when several point overlaps *i.e* when several simulation results are equal in filling efficiency for a same D_f value. Black crosses represent the mean of E_{fill} values for each D_f value. Dark crosses are connected by dashed lines to improve readability. (b) Particle trajectories and final positions for the most efficient disordered trap array with the optimised oblique cavity (corresponding to the highest point of Panel (a) with $D_f = 0.50$). The trapped particles and their trajectories are represented in red, the untrapped particle trajectories are represented in blue. The trapped particle diameter is increased to improve readability.

9.2.1 Disordered trap arrays can be easily expanded in the lateral direction

Disordered MTAs generate lateral dispersion of particles due to the trap relative positions. This characteristic offers more possibilities of the inlet/outlet channels and cavity designs than an optimised oblique chamber where all the five dimensionless parameters are fixed. As an example, we show here that when using the largest possible inlet/outlet channels ($Wch_r = 100\%$) and expanding the MTA size in the lateral direction, the filling and capture efficiencies are few modified and the averaged filling efficiency remains very close to 80% (Figure 11(a)) even though the MTA aspect ratio A_r and width ratio W_r are modified. The particle trajectories corresponding to largest chamber are shown Figure 11(b).

(a)



(b)

633 traps uniformly disordered chamber with $D_f = 0.40$

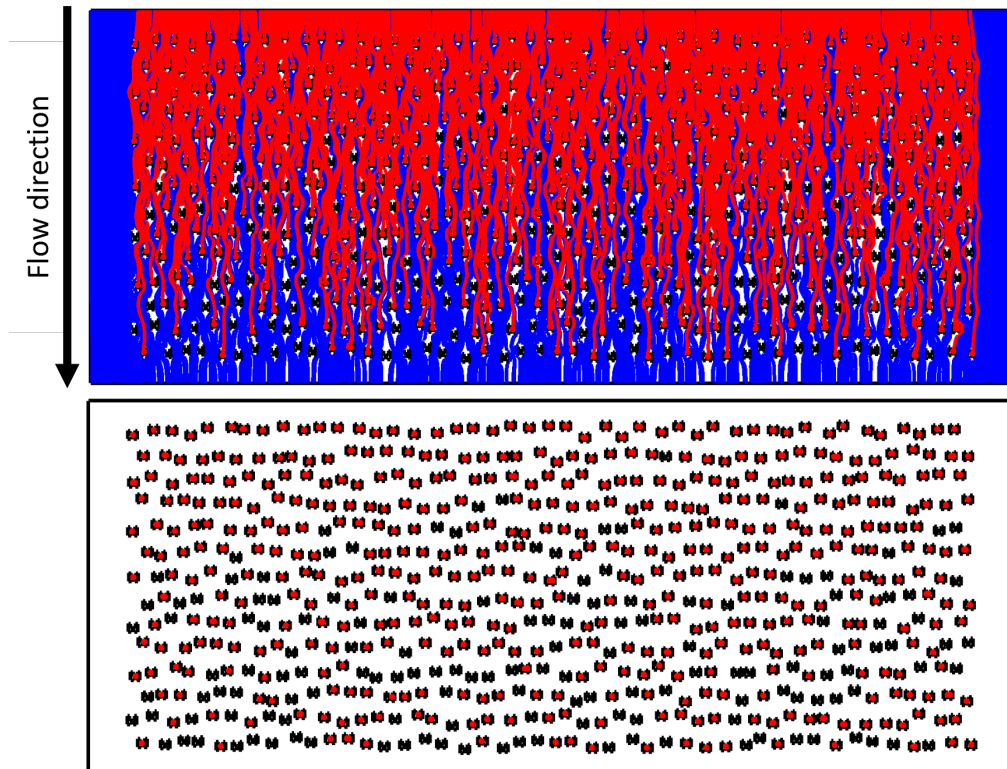


Figure 11: (a) Evolution of capture and filling efficiencies with respect to the number of traps when laterally expanding a $D_f = 0.40$ uniformly disordered MTA. Horizontal lines correspond to constant function least square fittings. (b) Particles trajectories in the biggest disordered MTA simulated on Panel (a). The trapped particles and their trajectories are represented in red, the untrapped particle trajectories are represented in blue. The trapped particle diameter is increased to improve visibility.